Applied Surface Science 505 (2020) 144008

Contents lists available at ScienceDirect

Applied Surface Science

journal homepage: www.elsevier.com/locate/apsusc

Full Length Article

Self-assembly of graphene sheets actuated by surface topological defects: Toward the fabrication of novel nanostructures and drug delivery devices

Yafei Wang[a], Changguo Wang[a,b,*]

[a] National Key Laboratory of Science and Technology for National Defence on Advanced Composites in Special Environments, Harbin Institute of Technology, Harbin 150001, PR China

[b] Center for Composite Materials, Harbin Institute of Technology, Harbin 150001, PR China

ARTICLE INFO

Keywords:
Self-assembly
Surface engineering and Reverse design
Graphene
Surface topological defects
Atomistic simulation

ABSTRACT

This paper focuses on self-assembly behaviors of graphene with surface topological defects using the atomistic simulation. The self-assembly graphene models are proposed based on three design principles. The systematic self-assembly simulations are performed and compared to achieve their dynamic nature and time dependence based on various design variables. It is found that the constructed self-assembly phase diagrams contain four distinct modes including polygon nanoscroll, polygon nanotube, breathing oscillation and damping vibration, which can be influenced by the number of unit cell along y-direction. Based on surface engineering consideration and reverse design paradigm, a target geometry such as polygon nanotube can be approximated by a graphene surface with programmable ripples and topological defects. Finally, the fundamental building block of self-assembly graphene is analyzed to reflect the self-assembly capacity. The results in this paper can be used to achieve the novel nanostructures and develop the design space of all-graphene-based drug delivery devices.

1. Introduction

Bending and folding endow everything around us in a position to under the rules of the game that natural law played ranging from spacetime ripples, folded mountains and brain wrinkles to corrugation surfaces of low dimensional materials. Emerging from the low dimensional materials, two dimensional (2D) graphene with fascinating honeycomb crystal lattice structure has attracted ever-increasing research interest as its exceptional mechanical properties, ultrahigh thermal conductivity and unique electronic transport [1–4]. The pristine sp^2-bonded hexagonal carbon lattice and signature electronic characteristics dominate the extreme thinness of monolayered graphene, and enable the superlative in-plane mechanical properties and ultra-low bending rigidity. Consequently, these constitute dramatic evidences that 2D graphene sheets can be transformed into novel three dimensional (3D) graphene nanostructures, exhibiting a wide range of applications including autonomous graphene origami robots [5,6], graphene high-frequency terahertz electromechanical devices [7,8], three dimensional (3D) graphene metamaterials [9], self-folding graphene nanocontainers for molecular mass storage [10,11] and drug delivery [12,13].

Self-assembly methods, i.e. spontaneous curving, folding or rolling-up of 2D graphene sheets, enable the surface topology modulation and transition. The last decade has seen rapid advancements in the field of graphene self-assembly based on surface engineering and functionalization, and several strategies motivated by experiments have been proposed to develop the self-assembly of graphene sheets. For the first self-assembly strategy, the 2D graphene sheets can be guided to self-assemble using inducer, which the capillary mechanism can guarantee the self-assembly of graphene [14–16]. The capillary forces are found to be induced by the carbon nanotube, fullerene, iron nanowire, water and ionic liquid [17,18]. Depending on the motif of graphene sheets prior to self-assembly, the nanoscroll, nano triangular pyramid and nano square prism are formed but filled with inducer. For the second self-assembly strategy, novel 3D graphene nanostructures are self-assembled from 2D graphene sheets through chemical functionalization [19,20]. Especially, doping atomic hydrogen to the carbon atoms in graphene and changing its hybridization from sp^2 to sp^3 with a lattice distortion open up a new pathway to driving the self-folding of graphene [21]. Zhang and coworkers unveiled the effect of hydrogenation pattern on graphene self-folding [12]. More recently, Zhu and coworkers studied the hydrogenation-assisted graphene origami [10]. The programmable tunability regarding graphene morphology enable an array of nanostructures of desired functionalities by design.

* Corresponding author at: National Key Laboratory of Science and Technology for National Defence on Advanced Composites in Special Environments, Harbin Institute of Technology, Harbin 150001, PR China.
E-mail address: wangcg@hit.edu.cn (C. Wang).

https://doi.org/10.1016/j.apsusc.2019.144008
Received 15 July 2019; Received in revised form 25 August 2019; Accepted 12 September 2019
Available online 26 November 2019
0169-4332/

Besides the abovementioned self-assembly strategies, surface topological defects are unavoidably introduced into graphene during the experimental process, topological defects including disclinations (-60° (pentagon) and $+60^{\circ}$ (heptagon) disclinations) and dislocations (heptagon-pentagon dipoles) are found to be most frequently ascertained when single-crystalline graphene fuses during the chemical vapor deposition (CVD) growth, or treatment using Scanning Focused Electron Beam Irradiation (SFEBI) [22]. The promising strategy regarding self-assembly of graphene with surface topological defects (or defect-controlled topological design in graphene) is of great important for self-assembling 2D graphene sheets into desirable 3D nanostructures [23,24]. The arrangement patterns of point defects and inverse Stone Wales defects in graphene prior to self-assembly have been proposed [25,26]. However, the research into self-assembly behaviors of graphene with surface topological defects, especially for disclinations and dislocations, is scarce. In addition, previous experimental and theoretical researches have indicated that surface topological defects have significant impacts on the nanostructure transitions with dynamic nature and time dependence [22]. However, the mechanisms for dynamic nature and time dependence of self-assembly graphene have not been well understood. It is of great significance to fully understand (a) the relationship between surface topological defects and dynamic nature and time dependence; (b) the underlying atomic-level mechanisms of surface topological defects on the graphene self-assembly properties.

Here, the present paper is organized in the following manner. Section 2 develops the methodology regarding design principles of self-assembly graphene model and simulation details. Section 3 systematically analyzes and discusses the self-assembly results from the aspect of dynamic nature and time dependence. Self-assembly phase diagrams are also conducted. Section 4 unveils the origin of self-assembly capacity, based on which the feasibility of drug delivery application is demonstrated. Section 5 recaps our motif and ends with a summary of the results.

2. Methodology

The current investigation involves sampling and analyzing 54 self-assembly graphene models (see Fig. S1–S2) to determine their self-assembly behaviors. A series of extensive atomistic simulations are performed to obtain the self-assembly properties and self-assembly phase diagrams. In this section, we systematically introduce the methodology with respect to atomic model establishment and simulation experiment.

In truly two-dimensional (2D) crystals (such as graphene), an edge dislocation with Burgers vector $\vec{b}$ is a topological defect where a semi-infinite strip of width $|\vec{b}|$ is embedded into a perfect 2D crystalline lattice [27], breaking the symmetry of translational invariance and distorting nearby planes of lattice in crystals [28]. With this guiding rule in hand, we construct each self-assembly graphene model by using surface topological defects. In current research, the synergy of three effects can guarantee the high self-assembly capacity. First, the self-assembly graphene should form high local deformation energy through geometry effect of topological defects. Second, the Burgers vectors $|\vec{b}|$ in a representative unit cell should cancel out each other to not cause the global distortion. Third, the graphene with surface topological defects should be "orthogonal anisotropy", resulting in directional self-assembly. Here we report the design of self-assembly graphene to meet those requirements. For a dislocation with the shortest Burgers vector ($|\vec{b}| = 2.46$ Å (angstrom)) in graphene lattice, it presents an edge-sharing pentagon-heptagon pair [27,29]. Whereas, as can be seen from Fig. 1, the representative unit cell of our self-assembly graphene contains two pentagons and two heptagons, L is the distance between pentagon and heptagon (see Fig. 1). We adopt a membrane theory approach [27] to establish this construction, i.e., a dislocation can be considered as a pair of -60° (pentagon) and $+60^{\circ}$ (heptagon) disclinations. If we "detach" the -60° disclination (or $+60^{\circ}$ disclination) from the dislocation, a larger dislocation with Burgers vector $|\vec{b}| = L$ ($=12.16$ Å > 2.46 Å) forms [29]. Due to the equal and opposite Burgers vectors in representative unit cell, the graphene lattice will not be distorted globally. Based on such a design paradigm, a series of self-assembly graphene nanostructures can be then described by density of unit cell and model length. We designate three degrees of freedom *DX*, *DY* and *N* in the design space of self-assembly graphene (see Fig. S2). The design variables *DX* (the first design variable) and *DY* (the second design variable) reflect the density of surface topological defects. The third design variable *N* represents the number of unit cell along y-direction. We give a symbol to characterize the three degrees of freedom in the design space: {*DX*, *DY*}&[*N*] represents the x-direction and y-direction length of self-assembly graphene are 5*DX* and *NDY*, respectively (*DX*: 34.3–51.1 Å, *DY*: 31.2–61.3 Å, *N*: 1–6). It is noteworthy that the initial configuration-optimized geometry characteristics of self-assembly graphene as schematically shown in Fig. 1 could be recorded as {42.6, 46.4}&[6].

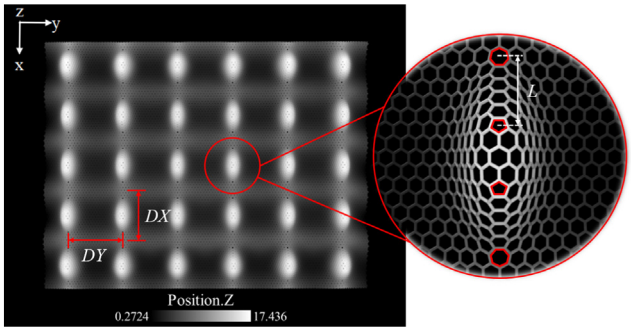

Fig. 1. Schematic illustration of graphene with surface topological defects. Each unit cell consists of two pentagon disclinations and two heptagon disclination. -60° (pentagon) disclination and $+60^{\circ}$ (heptagon) disclination can form a larger dislocation with Burgers vector $|\vec{b}| = L$ as compared with that of edge-sharing 5|7 dislocation. *DX* and *DY* can describe the density of topological defects. *N* represents the number of unit cell along y-direction. There are three freedom degrees (*DX*, *DY* and *N*) in the design space of graphene with surface topological defects. The geometry characteristics depicted in this section can be recorded as {42.6, 46.4}&[6].The legend shows the atomic coordinate of the z-direction that corresponds to the colour of atomic structures. (A colour version of this figure can be viewed online.)

To investigate the self-assembly behaviour of graphene with surface topological defects, all the extensive atomistic simulations are carried out using the Large-scale Atomic-Molecular Massively Parallel Simulator (LAMMPS) code package developed by Sandia National Laboratories [30]. The Adaptive Intermolecular Reactive Empirical Bond-Order (AIREBO) potential [31] is utilized to describe the interatomic interaction among carbon atoms. Due to the exclusively short-ranged REBO potential, AIREBO potential is very successful at describing the breaking and reforming covalent in various carbon system and predicting the mechanical properties of defective graphene [32–38]. For the parameter of short-ranges REBO potential in AIREBO potential functions, the cutoff distance is adjusted to 2.0 Å to avoid the spurious strengthening effects far beyond the initial elastic region [39] as suggested by Shenderova et al. [40]. Additionally, it is important to note that the Lennard-Jones term in AIREBO should be turned on to describe the corresponding interatomic van der Waals interaction.

Throughout the process of simulation experiment, a simulation box containing a self-assembly graphene can be established and periodic boundary conditions are applied in all three directions. The vacuum separation distance between self-assembly graphene and the edge of simulation box is 200 Å (for example, there is a 400 Å thick layer of empty space in z-direction), resulting in free movement of self-assembly graphene within the simulation box. This is conducive to the accurate

observation of self-assembly behavior for self-assembly graphene with different design variables. To stabilize the generated topological defects using Tool Command Language (TCL), all self-assembly graphene constructions are first quasi-statically optimized based on a Conjugated-Gradient (CG) algorithm to realize the local minimum energy configuration. Simulation experiments are carefully performed in the NVT (constant number of particles, constant volume and constant temperature) ensemble with a target temperature 300 K. The Nosé-Hoover thermostat is employed to control the temperature and generate the correct statistical ensemble. Standard velocity-Verlet integration algorithm is used in current research to integrate the equations of motion for the whole system. The time step is set to be 1 fs (femtosecond). Moreover, we also utilize 600 K to unveil the temperature impact of self-assembly behavior. The corresponding data can be carefully collected every 0.1 ps (picosecond) and all geometries depicted here are visualized using the open-source software OVITO. Each system is simulated long enough to achieve the equilibrium state.

3. Results and discussion

Previous studies [23,35] have demonstrated that the introduction of disclinations (negative disclination and positive disclination) and dislocations into graphene lattice can lead to extensively out-of-plane structural distortion. Pioneering experiments [1,22] using Scanning Focused Election Beam Irradiation (SFEBI) have been carried out on intentionally creating a large number of topological defects (such as dislocation) in a well-defined area of pristine monolayer graphene to induce the rippling graphene. Dynamic nature and time dependence of graphene with topological defects are far from being solved; the structural configuration transition or self-assembly behavior of defective graphene remains to be vivid and is still challenging.

This section we report how the “flat” self-assembly graphene surfaces can be transformed into useful three-dimensional (3D) structures and the final evolution modes and self-assembly phase diagrams of a family of self-assembly graphene are determined from simulation experiments. We demonstrate that graphene with different design variables can be programmed into a wide variety of target polygonal nanotubes. The breathing oscillation phenomenon and damping vibration phenomenon from self-assembly phase diagrams are discussed.

3.1. Transition from self-assembly graphene to nanoscroll

We first carried out systematic simulation experiments to explore the scrolling behaviors of a self-assembly graphene of a relative large of size with various design variables. Photographs of the final equilibrium morphologies for {42.6, 61.3}&[5] at 490 ps, {42.6, 61.3}&[6] at 500 ps and {51.1,41.4}&[6] at 500 ps are presented in Fig. 2(a)–(c). Notably, the graphene with topological defects can be transformed into nanoscroll with different core size on the basis of our three design principles. The z-direction sizes of {42.6, 61.3}&[5], {42.6, 61.3}&[6] and {51.1,41.4}&[6] structures are respectively 114.39 Å, 130.10 Å and 95.28 Å, which corresponds to the length of self-assembly graphene 306.50 Å, 367.80 Å and 278.40 Å. Fig. 2(d) from the top view reveals the sequential snapshots of self-assembly graphene with design variables {34.3, 31.2}&[6] at 0 ps, 15 ps, 50 ps, 80 ps, 100 ps, and 200 ps, respectively. The colour bar represents out-of-plane displacement field. At the beginning, the initial structure of self-assembly graphene {34.3, 31.2}&[6] is quasi-statically relaxed to reach the local minimum energy state (see the morphology at 0 ps in Fig. 2(d)). And then the self-assembly process starts from a curling motion of free edges, all four free edges of the rectangular region for self-assembly graphene curl up towards the opposite side of “rippling solitons” (see the morphology at 15 ps in Fig. 2(d)). The curling of the free edge along the direction of Burgers vector later becomes dominant mode, leading to the scrolling of the whole self-assembly graphene (see the morphologies from 50 ps to 100 ps in Fig. 2(d)), driven by geometry effect (as well as topology effect) of topological defects. When two free edges of self-assembly graphene start to contact (see 100 ps to 200 ps in Fig. 2(d)), surface tension can further propel the contacted free edges to slide with regard to each other, resulting in larger contact area. At the final stage of self-assembly, the system configurational entropy (i.e., freedom of nanoscroll with topological defects in the phase space) decreases due to the constraint of van der Waals interaction in contacted edges, and the whole self-assembly process finishes in 200 ps. After that, the system eventually reaches a thermodynamically stable nanoscroll phase at 300 K. It is important to note that the driven force for scroll phase of pristine graphene is van der Waals interaction between adjacent graphene layers. Whereas, the nanoscroll phase of graphene with surface topological defects is warranted by the “active folding” or curling rooted in geometry effect (as well as topology effect). The self-assembly mode and mechanism presented here is accordance with previous theoretical and experimental results regarding dynamic evolution of defective graphene, such as those for fabrication of carbon nanoscrolls from graphene with point defects reported by Sgouros [26], for spontaneous rolling-up of graphene with inverse Stone-Wales defects reported by Wang [25], for polarity dynamics of graphene defects reported by Pao [41], and for dynamic nature of rippling graphene through dislocation addition reported by Warner [22]. To further highlight this self-assembly mode, we perform simulations of pristine square graphene in Fig. 2(e), which has the similar size to self-assembly graphene structure {34.3, 31.2}&[6]. As evident in Fig. 2(e), out-of-plane fluctuations are typical configurations of membrane phase of graphene, which result from the synergy of in-plane stretching and out-of-plane bending modes. And the pristine graphene membrane reaches a thermodynamically stable state. From a mechanical point of view, the nanoscroll phase of self-assembly graphene is energetically more favourable than its basal planar form, considering the increasing deformation energy and van der Waals interaction energy. Accordingly, Fig. 2(f) provides the time dependence on variation of potential energy for {34.3, 31.2}&[6], {42.6, 61.3}&[5], {42.6, 61.3}&[6], {51.1, 41.4}&[6] self-assembly graphene and pristine graphene structures. Generally speaking, the potential energy variation as evident in Fig. 2(f) is highly correlated to the morphology evolution (see Figs. 2(a)–3(d)): first a linear decrease of curves due to quasi-statically relaxation followed by a sharp fluctuation from scrolling process, after which the variation of potential energy varies in a lesser extent because of thermodynamically stable state. It is apparent that variation of potential energy will increase if the density of topological defects increases as indicated in Fig. 2(f) (see curve {34.3, 31.2}&[6] and curve {51.1, 41.4}&[6]). When the density of topological defects is the same, such as {42.6, 61.3}&[5] and {42.6, 61.3}&[6] structures, with increasing of the self-assembly graphene length (i.e., the third design variable N) the variation of potential energy is increasing. These constitute dramatic evidences that large topological defect density and large self-assembly graphene length are the great motivators to enhance the deformation energy of graphene with surface topological defects. One can rationally utilize the additional impetus to develop the molecular detectors, molecular mass transportation system, nanoscale reaction vessels, storage vessel, reinforcement of nanocomposites, and drug delivery system [13,25,26]. However, for the pristine square graphene in Fig. 2(f) the potential energy variation is almost 0 eV. This indicates the pristine square graphene keeps a conformation of planar membrane instead of the self-assembly or self-folding (see Fig. 2(e)), which is in good agreement with previous experimental and computational results [42,43].

3.2. Transition from self-assembly graphene to nanotube

Prior studies has reported the effectiveness of defective graphene with point defect and inverse Stone-Wales defect in forming the stable nanotube. For example, it is suggested that heart-shaped nanotubes and circular nanotubes can be achieved using periodically placed bumps

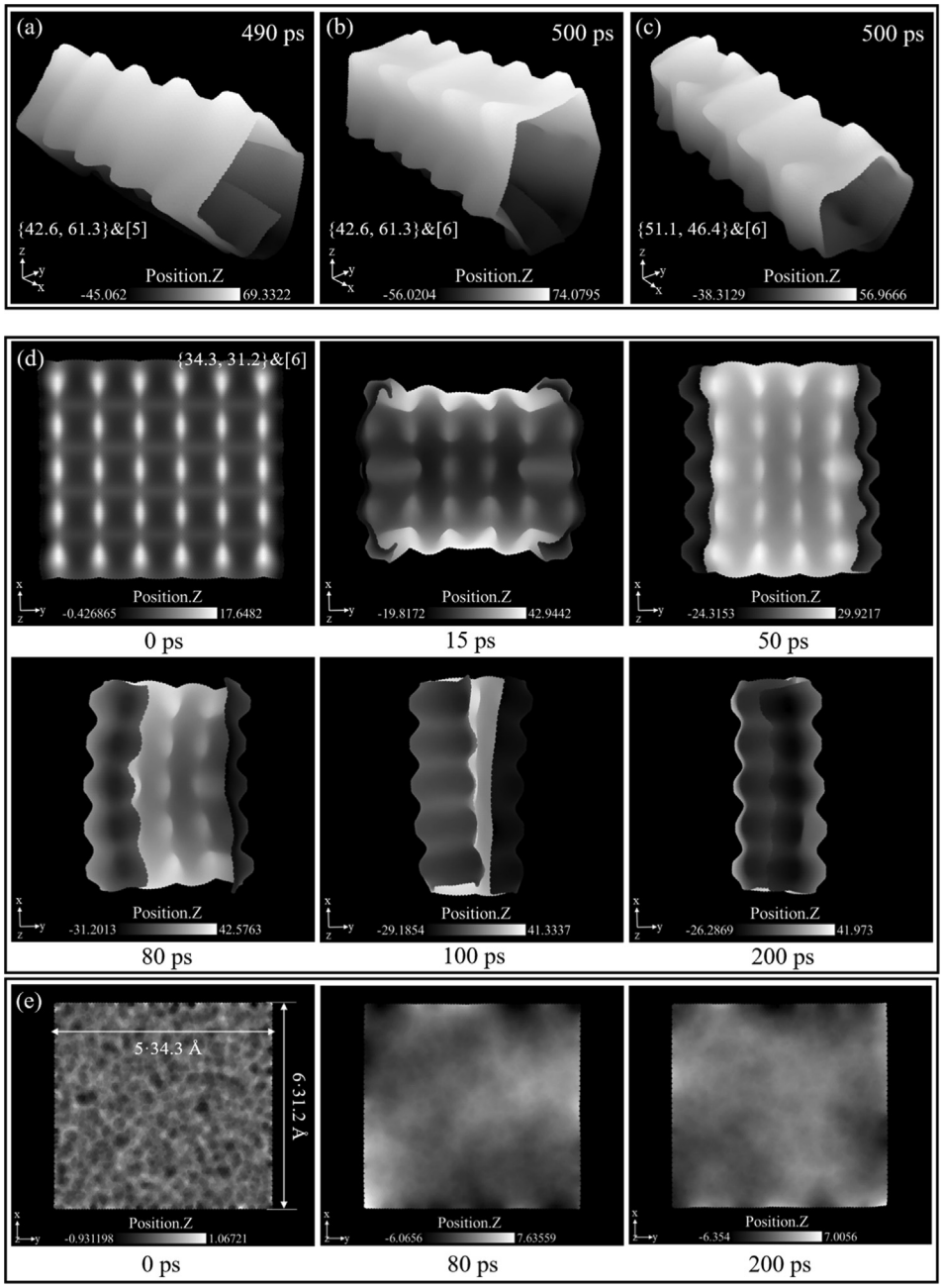

Fig. 2. Schematic illustration of the final equilibrium morphologies of self-assembly graphene structures for (a) {42.6, 61.3}&[5] at 490 ps, (b) {42.6, 61.3}&[6] at 500 ps and (c) {51.1, 41.4}&[6] at 500 ps, respectively. The geometries are presented in 3D view and colored according to the values of out-of-plane displacement. The colour bar represents the atomic coordinate of the z-direction. (d) Morphology evolution of {34.3, 31.2}&[6] self-assembly graphene structure at 0 ps, 15 ps, 50 ps, 80 ps, 100 ps, and 200 ps, respectively. Top view motifs of self-assembly graphene display self-assembly process. (e) Morphology evolution of pristine graphene structure with the similar size compared to {34.3, 31.2}&[6] at 0 ps, 80 ps and 200 ps, respectively. (f) Potential energy variation of four self-assembly graphene structures and pristine graphene as a function of simulation time. Variations in potential energy for {34.3, 31.2}&[6], {42.6, 61.3}&[5], {42.6, 61.3}&[6], {51.1, 41.4}&[6] and pristine graphene structures are plotted, respectively. (A colour version of this figure can be viewed online.)

with the complicated layout of inverse Stone-Wales (SW) defect [25]. However, identifying nanostructures that lead to nanotubes with desired geometries and functionalities presents a promising approach, and the key challenge is to bridge the vast design space of self-assembly from established structures to the overwhelming complexity of the targeted geometries.

In this subsection, we utilizing several simulation experiments demonstrate the importance of graphene with surface topological defects in transforming into the stable nanotube with desired geometries. The dynamic characteristics and time dependence of self-assembly graphene are investigated, which allows us to obtain a richer insights into self-assembly behaviors. Emerging from Fig. 3 is the feasible ways of simulating the formation of a given polygon tube based on self-assembly. Photographs of the evolutionary equilibrium morphologies (300 K) for self-assembly graphene with design variables {34.3, 31.2}&[3] at 516 ps, {42.6, 46.4}&[4] at 503 ps and {34.3, 64.3}&[5] at 557.3 ps are illustrated in Fig. 3(a)–(c). Obviously, adding “rippling soliton” with well-defined topological defects throughout the whole graphene can lead to the controllable formation of nanotube. The cross-section shapes of nanotube from self-assembly graphene resemble a triangle, square and pentagon, which the corresponding side lengths are 31.2 Å, 46.4 Å and 64.3 Å, respectively, i.e., the second design variable *DY*. Therefore

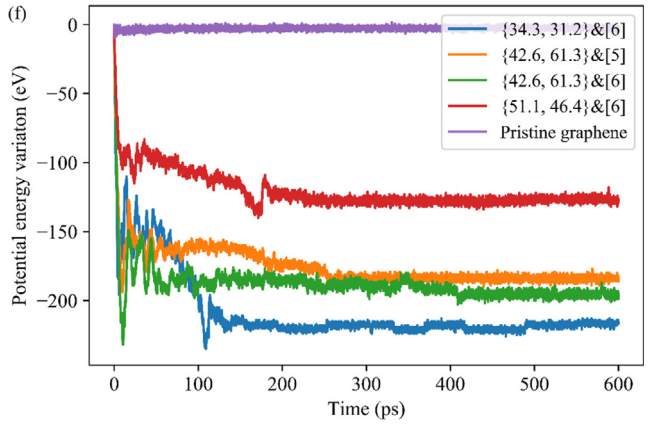

Fig. 2. (*continued*)

it is straightforward to reverse engineer a "flat" self-assembly graphene surface with surface topological defects to approximate a target geometry. The essence of this construction is that after designating the specific density of topological defects and identifying the dominant factor of *N* we have a surface with *N* "rippling crease", which can cause the surface to buckle into an *N* gon nanotube.

As a demonstration, Fig. 3(d) from the top view shows a sequence of self-assembly process snapshots of hexagon nanotube for {51.1, 31.2}&[6] self-assembly graphene structure, where morphologies and out-of-plane displacement field are captured under 0 ps, 30 ps, 50 ps, 69 ps, 74.9 ps and 100 ps, respectively. As before, initially established model of {51.1, 31.2}&[6] self-assembly graphene should be quasi-statically optimized to reach the local minimum energy configuration (see the morphology at 0 ps in Fig. 3(d)). Due to the geometry effect (and topological effect) of topological defects, the self-assembly graphene will spontaneously generate out-of-plane perturbation (see the morphology at 30 ps in Fig. 3(d)), and then continuous scrolling of free edges with armchair chiralities along the direction of Burgers vector proceed (see the morphologies from 50 ps to 69 ps in Fig. 3(d)). When two parts of the self-assembly graphene start to meet after an initially directional self-assembly process, extremely delicate oscillations of the self-assembly structure induce chemical reaction between nearby boundaries, leading to the formation of carbon–carbon covalent bond and the transition of self-assembly graphene into nanotube (see the morphologies from 74.9 ps to 100 ps in Fig. 3(d)). Here, the suture phenomenon of self-assembly graphene is essentially identical to that considered in the previous computational and experimental studies for self-assembly of defective graphene [25,26,44–46]. Note that carbon exhibits a very abundant dynamic process of bond-breaking and bond-reforming [34], while the formation of nanotube is completely seamless, as indicated in Fig. 3(d).

To gain the detailed physical insights into the atomic-level suture mechanisms, Fig. 3(e) provides the potential energy landscape as a function of x coordinates and y coordinates when dynamic formation of carbon-carbon bonds from 69 ps, 74.9 ps, 78.5 ps to 100 ps, which corresponds to the morphology evolution of hexagon nanotube from self-assembly graphene, as evident in Fig. 3(d) (see the morphologies from 69 ps to 100 ps). The colour bar represents the specific atomic potential. The counterintuitive black zone at 100 ps in Fig. 3(e) represents the surface defect of nanotube. It can be observed that dynamic suture starts from a chemical reaction from one end with negative x-coordinates of self-assembly graphene (see 69–74.9 ps in Fig. 3(e)). Once the first pair of covalent bonds forms, the successive chemical reaction of the neighboring segments will be triggered (see 74.9–78.5 ps in Fig. 3(e)). We use a dominolike bonding effect to describe this successive formation of carbon-carbon covalent bonds. The propagation of "domino wave" along the x-direction can be found accordingly, which the corresponding propagation speed changes nonlinearly with the simulation time. Important progress can be made by realizing that carbon atoms with high potential energy ~ -5 eV for free boundaries can transform into sp^2-hybridized atoms with low potential energy ~ -7.5 eV, schematically shown in Fig. 3(e). With the domino bonding effect, the novel nanostructure (hexagon nanotube) can be achieved using graphene with surface topological defects. Apart from the potential applications [13,25,26] as mentioned above, these novel nanostructures may exert vigorous driving force on enhancing the scalability of design space of new nanodevices in relation to mechanics and condensed matter physics. For example, one can utilize the novel *N* gon nanotubes to design a thermal management device. The low thermal conductivity of thermal modulator may be responsible for the phonon scattering from "rippling surfaces" and topological defects (negative/positive disclination) [47]. In future, we hope special care should be taken when surface rippling plays a more important role in the new generation of graphene-based nanodevices. Fig. 3(f) provides the snapshots of graphene membrane phase with out-of-plane thermal fluctuations. The geometrical sizes are similar to that of self-assembly graphene {51.1, 31.2}&[6], but the self-assembly will not occur. This indirectly reflects that surface topological defects can effectively actuate the graphene sheets. Equally, the promising graphene origami can be realized based on this design strategy.

Fig. 3(g) reveals the evolution of the system potential energy of {34.3, 31.2}&[3] (including the time dependence on variation of potential energy at 600 K), {42.6, 46.4}&[4], {34.3, 64.3}&[5], {51.1, 31.2}&[6] self-assembly graphene and pristine graphene structures. It indicates that pristine graphene in membrane phase presents a thermodynamically stable state, and for self-assembly graphene variation in potential energy is closely associated with their self-assembly process as can be seen in Fig. 3(a)–(d): first, applied Conjugated-Gradient (CG) algorithm can relax in-plane constraints from model establishment based on Tool Command Language (TCL), and causes a moderate drop of the potential energy curve at the initial stage; second, a large amplitude bending motion triggered by out-of-plane perturbation can increase the deformation energy of self-assembly graphene, resulting in the fluctuant decreasing of potential energy; third, chemical reaction occurs based on domino bonding effect, leading to drastic decline of potential energy curve; finally, dynamic suture process can realize the thermodynamically stable state of nanotube from self-assembly graphene, as we can see in Fig. 3(g). Additionally, Fig. 3(g) reveals that the potential energy variation can be strongly influenced by the total number of atoms and system sizes, based on which the largest variation of potential energy (up to 600 eV) from {51.1, 31.2}&[6] self-assembly graphene structure can be attributed to the largest number of atoms of 21,420.

We also investigate the temperature impact of self-assembly behavior. The acceleration effect of self-assembly is investigated using {34.3, 31.2}&[3] self-assembly graphene at 300 K and 600 K (see Fig. 3(g)), respectively. We find that with increasing of temperature (< a certain critical temperature) the self-assembly efficiency is increasing, i.e., {34.3, 31.2}&[3] self-assembly graphene at 600 K can be transformed into nanotube faster than that of 300 K ($t_{600K} < t_{300K}$). Here, we qualitatively reveal the insights into the acceleration effect of self-assembly based on theory of thermodynamics. And two important conclusions should be refined: first, the "flat" self-assembly graphene has a larger free energy (*F*) as compared with that of self-assembly graphene with a large amplitude bending motion at 0 K; second, the self-assembly graphene with bending motion is more unconstrained, leading to more freedom in the phase space, which the entropy (*S*) of self-assembly graphene with bending motion is larger than "flat" self-assembly graphene. Combining $F = E - TS$ and $dF = -SdT$, it is apparent that the free energy of both "flat" self-assembly graphene and self-assembly graphene with bending motion will decrease if temperature increases. Whereas, the free energy of "flat" self-assembly graphene decreases slower, which can directly result in the increasing of free energy variation (see Fig. S3). This mechanism can guarantee the

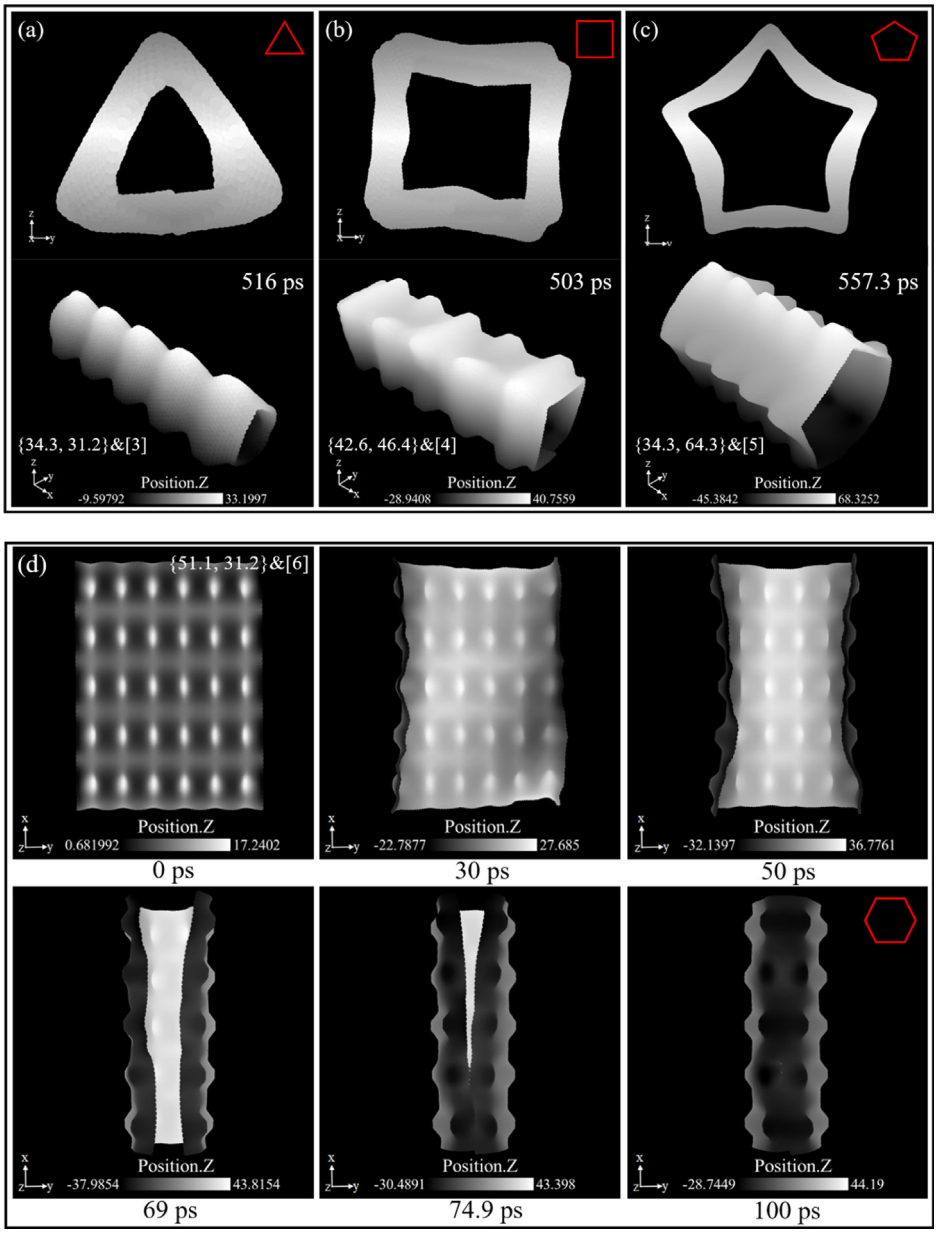

Fig. 3. Schematic illustration of the final equilibrium morphologies of self-assembly graphene structures for (a) {34.3, 31.2}&[3] at 516 ps, (b) {42.6, 46.4}&[4] at 503 ps and (c) {34.3, 64.3}&[5] at 557.3 ps, respectively. These morphologies are presented in the side view and 3D view. In the simulation experiments of (a), (b) and (c), the self-assembly graphene can be successfully transformed into novel N gon nanotubes, which the corresponding cross-section shapes resemble a triangle, square and pentagon with side lengths 31.2 Å, 46.4 Å and 64.3 Å, respectively. The geometries are colored according to the values of out-of-plane displacement. The colour bar represents the atomic coordinate of the z-direction. (d) Morphology evolution of self-assembly graphene with design variables {51.1, 31.2}&[6] at 0 ps, 30 ps, 50 ps, 69 ps, 74.9 ps, and 100 ps, respectively. Top view motifs of self-assembly graphene display self-assembly process and the final morphology resembles a hexagon nanotube. The colour bar represents the z-directional coordinate of atoms. (e) Potential energy landscape as a function of × coordinates and y coordinates at 69 ps, 74.9 ps, 78.5 ps and 100 ps. The colour bar represents the specific atomic potential. The counterintuitive black zone at 100 ps represents the surface defect of hexagon nanotube. (f) Morphology evolution of pristine graphene with the similar size to {51.1, 31.2}&[6] at 0 ps, 50 ps, 69 ps and 100 ps, respectively. (g) Time dependence on potential energy variation for self-assembly graphene with design variables {34.3, 31.2}&[3], {42.6, 46.4}&[4], {34.3, 64.3}&[5], {51.1, 31.2}&[6] and pristine graphene. Potential energy variation of {34.3, 31.2}&[3] self-assembly graphene structure at 600 K is also investigated. (A colour version of this figure can be viewed online.)

acceleration effect of self-assembly and be conducive to guide the morphology controlling of generated nanodevices based on self-assembly graphene. In other words, this finding shows that we can control the self-assembly efficiency by controlling the temperature.

3.3. Self-assembly phase diagrams: Breaking the governing mechanism for geometry-controlled configuration of graphene

In this subsection, we systematically conduct 54 independent simulation experiments and summarize the most probable final morphologies. As can be identified in Fig. 4, the phase diagrams of the final evolution modes of self-assembly graphene are presented in the parametric space of the number of unit cell N (=1, 2, 3, 4, 5 and 6) and y-direction length of unit cell DY (=31.2 Å, 46.4 Å and 61.3 Å), for a given DX (=34.3 Å, 42.6 Å and 51.1 Å). We define the corresponding modes (Mode I, Mode II, Mode III and Mode IV) of evolution as polygon nanoscroll (see Section 3.1), polygon nanotube (see Section 3.2), breathing oscillation and damping vibration, respectively. The results

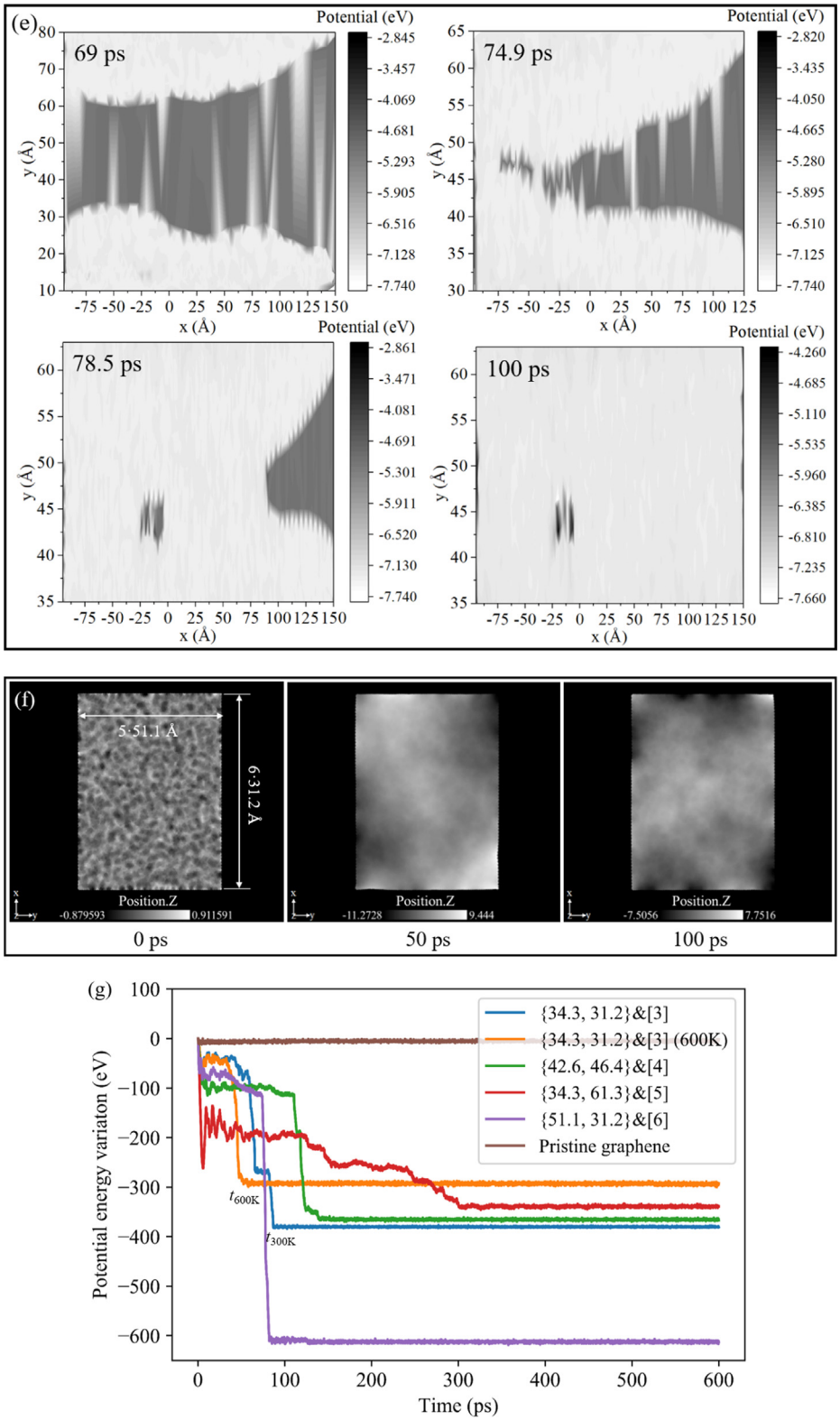

Fig. 3. (*continued*)

of simulation experiments, as listed in Fig. 2(a)–(d) and Fig. 3(a)–(d), are also prepared and compared in the phase diagrams. The most comprehensive understanding stemmed from Fig. 4(a)–(c) is that for a specific density (*DX* and *DY*) of topological defects self-assembly graphene can be transformed into four different morphologies which are found to be strongly influenced by the third design variable *N*. Three threshold values of the third design variable *N* can be determined: $N_{Threshold\text{-}1}$, $N_{Threshold\text{-}2}$ and $N_{Threshold\text{-}3}$ represent the morphology thresholds between Mode IV damping vibration and Mode III breathing oscillation, Mode III breathing oscillation and Mode II polygon nanotube, and Mode II polygon nanotube and Mode I polygon nanoscroll, respectively. It is conceivable that with increasing of the third design variable *N* morphology mode will successively bridge the morphology thresholds (from $N_{Threshold\text{-}1}$ to $N_{Threshold\text{-}2}$ to $N_{Threshold\text{-}3}$), leading to our

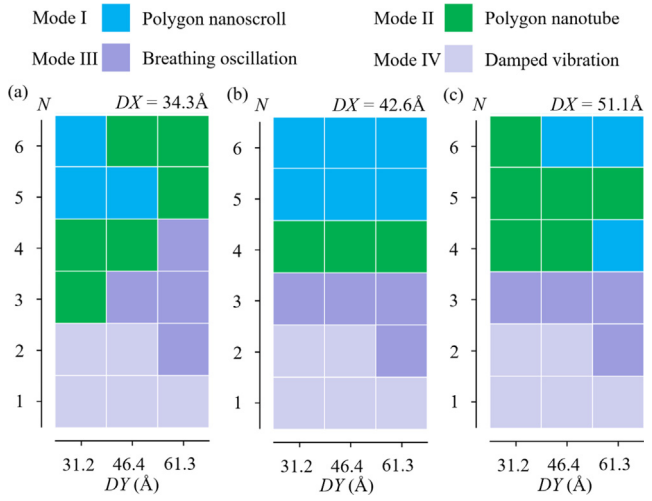

Fig. 4. Phase diagrams of the four final morphology modes of self-assembly graphene in the parametric space of the number of unit cell N (=1, 2, 3, 4, 5 and 6) and y-direction length of unit cell DY (=31.2 Å, 46.4 Å and 61.3 Å), for a given design variables (a) DX = 34.3 Å, (b) DX = 42.6 Å and (c) DX = 51.1 Å). Evolutionary Mode I, Mode II, Mode III and Mode IV are defined as polygon nanoscroll, polygon nanotube, breathing oscillation and damping vibration, respectively. (A colour version of this figure can be viewed online.)

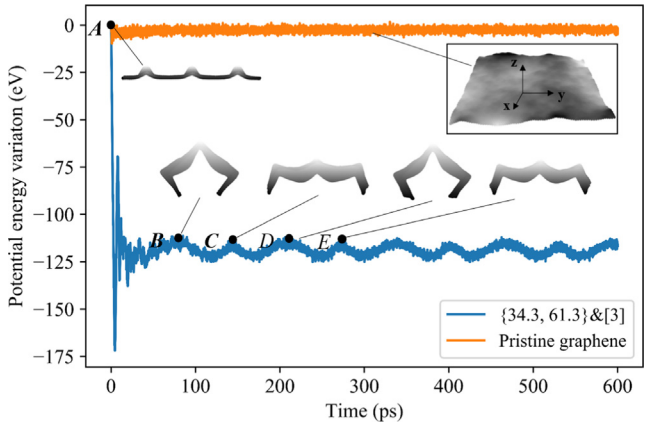

Fig. 5. Breathing oscillation of self-assembly graphene with design variables {34.3, 61.3}&[3]. Simulation experiment results for the evolution of potential energy of self-assembly graphene and pristine graphene as a function of time are provided. The morphology evolution (morphology *A*, *B*, *C*, *D* and *E*) of self-assembly graphene is presented in legend, which respectively correspond to the marked points *A*, *B*, *C*, *D* and *E*. (A colour version of this figure can be viewed online.)

workable and programmable design paradigm. It is extremely probable that for a given DX (the first design variable) the morphology threshold is increasing with increasing of the second design variable DY. We note that our programmable designs of self-assembly graphene are superior to many designs for comparable results, especially with respect to self-assembly. More importantly, the results emerging from the phase diagrams indicate that our design breaks the governing mechanism for geometry-controlled configuration of graphene sheets. According to the Mermin-Wagner theorem, the long-range order of 2D crystals can be destroyed by long wavelength, resulting in the crumpled tendency of 2D membranes in a 3D space [48]. In graphene sheets, the anharmonic coupling between bending mode and stretching mode can suppress those dangerous fluctuations and stabilize the flat geometry of graphene. It is reported that when the length and width of graphene are the similar (or the aspect ratio: length/width $<$ 10), the graphene sheet will keep a configuration of planar membrane [42]. For our phase diagrams in the parametric space, however, it is obvious that graphene with topological defects surpass this governing mechanism. For example, the aspect ratio of {34.3, 31.2}&[5] and {42.6, 46.4}&[4] structures are both smaller than 10, but the correspondingly thermodynamically stable states are polygon nanoscroll and polygon nanotube, respectively. Equally, simulation experiments of the multipotent nanoscroll and nanotube can make it clear that in our self-assembly graphene constructions the self-assembly process is extremely robust. Beside this, inspection of broader landscapes from the phase diagrams is performed, we find that the self-assembly graphene with breathing oscillation and damping vibration can be ingeniously devised, accomplished by decreasing the third design variable N. Based on their dynamic characteristics, the self-assembly graphene in relation to Mode III breathing oscillation and Mode IV damping vibration might be important for the application of graphene-based nanomechanical devices such as nanoactuators, nanorobots, and nanooscillators [49]. Next, we report the importance of breathing oscillation phenomenon and damping vibration phenomenon.

3.3.1. Breathing oscillation phenomenon of self-assembly graphene

Recent developments in breathing oscillation of carbon nanoscrolls have stimulated interest in regard to nanooscillators capable of operating at controllable conditions. However, the need for defective graphene capable of achieving the breathing oscillation while providing for adequate robustness has not led to a consideration of surface topology design. Here, we demonstrated breathing oscillation of self-assembly graphene can be enabled by topological defects of surface. As is evident from the landscape of self-assembly phase diagram (see Fig. 4) that for a specific density of topological defects self-assembly graphene will present the breathing oscillation phenomenon, which the third design variable N is ranged between morphology threshold $N_{Threshold\text{-}1}$ and $N_{Threshold\text{-}2}$. To unveil the underlying mechanism and the characteristics of breathing oscillation, Fig. 5 provides the representative schematic evolutions of potential energy based on self-assembly graphene {34.3, 61.3}&[3] and similar sized pristine graphene structures. Roughly, the potential energy variation of pristine graphene is 0 eV, and the whole breathing oscillation process for self-assembly graphene {34.3, 61.3}&[3] can be divided into two stages. At the beginning of simulation experiments, the potential energy curve quickly decreases to a relative low level which gives the self-assembly graphene a local minimum energy configuration. After that the potential energy curve slightly increases and breathing oscillation phenomenon occurs. At the second stage, the potential energy changes periodically and keeps the constant oscillation frequency and oscillation amplitude for a long time. The representative morphologies of self-assembly graphene are labelled in legend, which correspond to the marked points *A*, *B*, *C*, *D* and *E*, respectively. From an energy point of view, breathing oscillation phenomenon is responsible for the energy conversion and energy dissipation. At point *A* of the first stage, the potential energy stored in the self-assembly graphene can be expressed as

$$E^{P-A} = E_{L-A} \tag{1}$$

where $E_{L\text{-}A}$ is the local deformation energy from topological defects design. After the quasi-statically optimized process, the potential energy at point *B*, *C*, *D* and *E* of the second stage can be written as

$$E^{P-i} = E_{L-i} + E_{G-i} (i = B, C, D, E) \tag{2}$$

where $E_{L\text{-}i}$ and $E_{G\text{-}i}$ represent the local deformation energy and global deformation energy of self-assembly graphene at point i = *B*, *C*, *D*, *E*, respectively. According to the principle of energy conservation, the energy from point *A* to point *B* can be given using the following relationship

$$E^{P-A} = E^{P-B} + E^{Dissipation} \tag{3}$$

where $E^{Dissipation}$ represents the energy dissipation to environment. The energy relationship at point *B*, *C*, *D* and *E* can be determined using a continued equality

$$E^{P-B} = E^{P-C} = E^{P-D} = E^{P-E} \tag{4}$$

Concretely speaking, at the first stage (see point *A* to point *B*), the initial potential energy $E^{P\text{-}A}$ decreases and converts into kinetic energy, followed by a tremendous energy dissipation due to kinetic energy, after which absorbing energy from the environment leads to the energy enhancement of self-assembly graphene and the potential energy $E^{P\text{-}B}$ of point *B*. In this process, local deformation energy $E_{L\text{-}A}$ is mostly dissipated and partially converted into global deformation energy $E_{G\text{-}B}$, the finally remaining energy is retained which is the energy $E_{L\text{-}B}$. At the second stage, breathing oscillation of self-assembly graphene can be guaranteed using equivalent energy conversion. For example, from point *B* to point *C* the global deformation energy $E_{G\text{-}B}$ decreases with the opening expansion of self-assembly graphene (see morphology *B* to morphology *C* in Fig. 5, the mean curvature of self-assembly graphene decreases with the opening expansion). Decreasing of global deformation energy can be given by

$$\Delta E_{G-B-C} = E_{G-B} - E_{G-C} \tag{5}$$

Correspondingly, increasing of local deformation energy can be expressed by

$$\Delta E_{L-B-C} = E_{L-C} - E_{L-B} \tag{6}$$

where the energy variations in global deformation energy and local deformation energy are equivalent, i.e., $\Delta E_{G\text{-}B\text{-}C} = \Delta E_{L\text{-}B\text{-}C}$. Through a sequence of energy converting, breathing oscillation of self-assembly graphene can be realized. For completeness, we also investigate the effect of the third design variable *N* on the oscillation frequency and oscillation amplitude. As detailed in Fig. S4, we provide the potential energy evolutions of self-assembly graphene with design variables {34.3, 61.3}&[3] and {34.3, 61.3}&[4]. It is apparent that breathing oscillation process of self-assembly graphene structure {34.3, 61.3}&[4] is similar to that of {34.3, 61.3}&[3] and also has two distinct stages. With increasing of the third design variable *N* the oscillation frequency and oscillation amplitude are decreasing. It is noteworthy that the resultant breathing oscillation phenomenon (at 300 K) is energetically robust against the thermal perturbations. Additionally, an attractive but relatively unexplored area is the realization of reconfigurable self-assembly graphene structure that can expand and shrink at specific locations or in response to external stimuli to enable nanoactuator and nanorobot.

3.3.2. *Damping vibration phenomenon of self-assembly graphene*

Damping of graphene has significant applications in nanodevices and dynamic systems for absorbing the shock-induced energies [3,8,50]. In contrast to those available damping studies in relation to pristine graphene, in current research we introduce the damping vibration phenomenon of graphene with topological defects. According to self-assembly phase diagrams in Fig. 4 the damping vibration tends to occur when the third design variable *N* is lower than the morphology threshold $N_{Threshold\text{-}1}$. As a demonstration, damping vibration behavior of self-assembly graphene {34.3, 31.2}&[1] is presented, followed by a mechanism explanation using the principle of energy. In general, the damping will govern the energy dissipation throughout the whole vibration process. It is seen from Fig. 6(a) that the evolution of potential energy for self-assembly graphene {34.3, 31.2}&[1] is time-dependent, with time increasing the vibration amplitude is gradually decreasing due to damping of self-assembly graphene. Fig. 6(b) gives us a lesser extent with respect to simulation time from 0 ps to 90 ps. The more friendly landscape allows us to focus and then gain deeper insight into the damping vibration of self-assembly graphene. The typical morphology evolutions (morphologies *a*, *b*, *c*, *d*, *e* and *f*) are provided in legend, corresponding to the marked points *a*, *b*, *c*, *d*, *e* and *f*, respectively. Specifically, from point *a* to point *b*, the decreasing potential energy converts into kinetic energy, and the energy dissipates through kinetic energy into the environment. When potential energy curve goes into the second regime (from point *b* to point *c*), the self-assembly

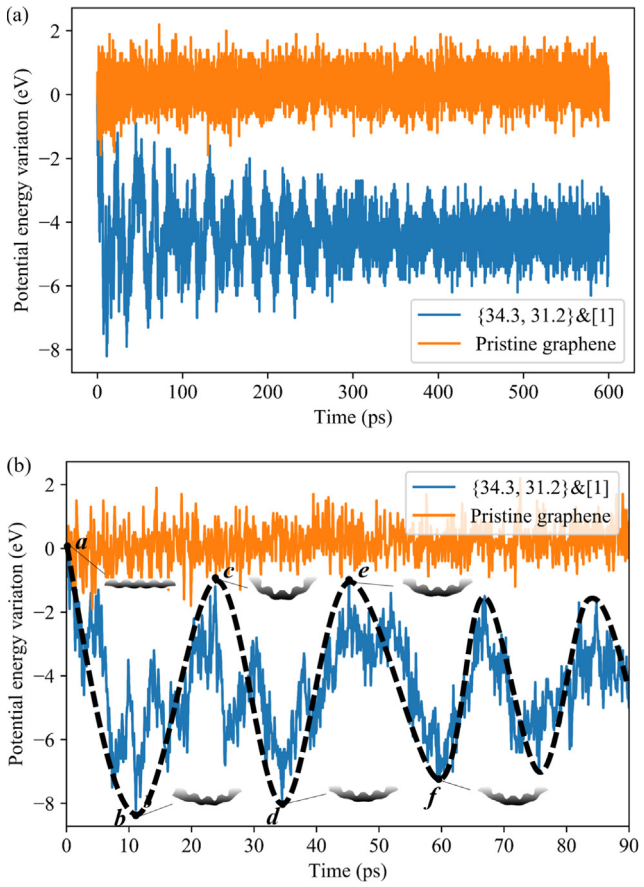

Fig. 6. Damping vibration of self-assembly graphene with design variables {34.3, 31.2}&[1]. (a) Evolution of potential energy as a function of time from 0 ps to 600 ps. The whole process of evolution is governed by damping of self-assembly graphene. (b) Evolution of potential energy with a lesser extent with respect to simulation time from 0 ps to 90 ps. (A colour version of this figure can be viewed online.)

graphene starts to absorb energy from the environment, and the potential energy is increasing. It is apparent that the initial local deformation energy (at point *a*) is partially dissipated into environment and partially converted into global deformation energy, leading to the potential energy at point *c* is smaller than that of point *a*. Therefore, the energy exchange between self-assembly graphene and environment from energy dissipation and energy absorption is lopsided, showing the non-recoverable potential energy dissipation [25], resulting in the decreasing of vibration amplitude of potential energy. The energy relationship between point *a*, *c* and *e* can be given using the following continued equality

$$E^{P-a} = E^{P-c} + E^{Dissipation-a-c} = E^{P-e} + E^{Dissipation-a-c} + E^{Dissipation-c-e} = \cdots \tag{7}$$

where $E^{P\text{-}a}$, $E^{P\text{-}c}$ and $E^{P\text{-}e}$ represent the energy at point *a*, *c* and *e*, respectively. $E^{Dissipation\text{-}a\text{-}c}$ and $E^{Dissipation\text{-}c\text{-}e}$ represent the energy dissipation to environment from point *a* to *c* and point *c* to *e*, separately. Notably, through a successive energy dissipation (*a*-*b*-*c*-*d*-*e*-*f* …), damping vibration of self-assembly rippling graphene can be achieved. At the final stage of damping vibration, the self-assembly graphene presents a relative stable state. This damping vibration phenomenon is nominally consistent with previous finding with regard to defective graphene given in those of Wang [25]. Additionally, we also investigate the impact of the third design variable *N* on the vibration frequency and vibration amplitude of self-assembly graphene with design variables {34.3, 31.2}&[1] and {34.3, 31.2}&[2], as we can see in Fig. S5. It is widely accepted that the vibration frequency and vibration amplitude

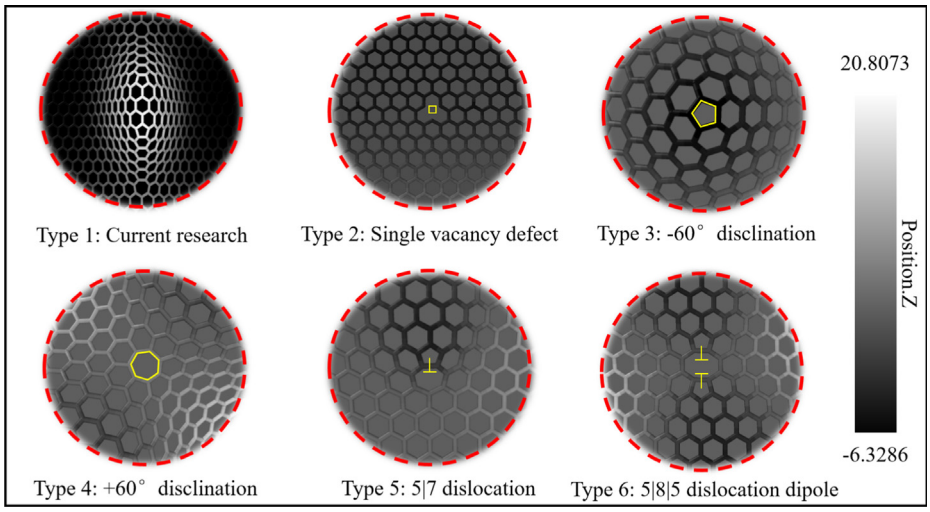

Fig. 7. Illustration of 6 fundamental building blocks with respect to topological defects: a representative unit cell of self-assembly graphene with two pentagons and two heptagons (Type 1), single vacancy defect (Type 2), −60° disclination (Type 3), +60° disclination (Type 4), 5|7 dislocation (Type 5), and 5|8|5 dislocation dipole (Type 6). The colour bar represents the out-of-plane displacement field. (A colour version of this figure can be viewed online.)

will increase if the third design variable N increases. It is important to note that the final morphology of self-assembly graphene is vulnerable to thermal perturbations.

4. Self-assembly capacity and potential application: Insights from the fundamental building block

4.1. Comparison of energy for diverse topological defects

From an energetic point of view, achieving high self-assembly capacity of graphene requires an extremely large driving force to bridge the deformation energy barrier (such as $\int_A D\kappa^2(x, y)dxdy/2$, D and κ represent the bending rigidity and mean curvature, respectively). Although to some extent topological defects limit the mechanical performance of graphene, the duality of topological defects can make it possible to induce the geometric distortion of graphene, leading to especially dominant local response to overcome the energy barrier. This is also the core design approach of our self-assembly research. Equipped with an efficient mapping between the topological defect and its geometry effect (see Figs. S6 and S7), we consider 6 fundamental building blocks in relation to topological defects as indicated in Fig. 7, including the representative unit cell (i.e., the building block) of our self-assembly graphene with two pentagons (−60° disclinations) and two heptagons (+60° disclinations) (Type 1), single vacancy defect (Type 2), −60° disclination with positive Gaussian curvature (Type 3), +60° disclination with negative Gaussian curvature (Type 4), 5|7 dislocation or disclination dipole (Type 5), and 5|8|5 dislocation dipole (Type 6). The colour bar applies to Type 1 to Type 6 in Fig. 7, and indicates the out-of-plane displacement field. To better characterize the self-assembly capacity of our self-assembly graphene, Table 1 provides the comparison of incremental atomic potential energy of 6 fundamental building blocks and the unit cell with 1–6 inverse Stone-Wales defects in Refs. [25]. Here, incremental atomic potential energy E_{LAPE} is given by

$$E_{IAPE} = \frac{||E_{PGS}| - |E_{TDS}||}{|E_{PGS}|} \times 100\% \quad (8)$$

where E_{PGS} represents the potential energy per atom of pristine graphene, E_{TDS} represents the potential energy per atom of topological defects. Obviously, the building block of graphene with surface topological defects has the largest incremental atomic potential energy E_{LAPE} within the studied range, this could be nearly 8 times larger than Type 2 single vacancy defect. The E_{LAPE} of Type 1 topological defect would be as many as ~3.38%, i.e., our novel design can lead to ~3.38% increase in potential energy per atom as compared with that of pristine graphene. This finding is remarkable and is comparable to ones ~2.70% in other studies of the self-assembly defective graphene [25]. Combining three design principles proposed in Section 2, this observation directly demonstrates that larger deformation energy can be stored in self-assembly graphene, resulting in the high self-assembly capacity and directionally preferential capacity. With these advantages in hand, the combination of fundamental building blocks to programmatically replicate the “ripples” can lead to a framework in which desired self-assembly capacity of graphene can be designed rationally.

4.2. Direct evidence of self-assembly behavior: folding effect

To showcase the full potential of graphene with topological defects and the direct evidence of self-assembly behavior (see Figs. S8, S9 and S11), the folding effect of self-assembly graphene will be straightforward unveiled in this subsection. As a demonstration, a unit cell from self-assembly graphene {42.6, 46.4}&[5] in the phase diagram Fig. 4(b) can be designated to determine the folding effect (we symmetrically delete some atoms in the boundaries and let $DX \approx DY \approx 42.6$ Å). We begin by introducing the corresponding simulation experiment methods. Concretely speaking, two independent simulation experiments are conducted to identify the folding effect: the self-assembly graphene unit cell with end restrained, and the spontaneous folding of self-assembly graphene along the direction of Burgers vector (see Fig. 8(a)). For the former experiment, the specimen of self-assembly graphene unit cell is carefully clamped with virtual antiskid in LAMMPS, and then the potential energy variation is measured as precisely as possible. A strain ratio of zero is used which produced the exact evolution curves. For the second simulation experiment with respect to spontaneous folding, it is, in fact, implemented as a benchmark experiment. If two sets of experimental data in relation to the variation of potential energy and stress are found to be remarkably different, our

Table 1
Comparison of incremental atomic potential energy for diverse topological defects, indicating that larger deformation energy can be stored in self-assembly graphene.

	Type1	Type2	Type3	Type4	Type5	Type6	Graphene	Ref.[25]
E_{LAPE} (%)	3.38	0.14	2.84	2.57	2.57	2.84	0	up to 2.70
E_{TDS} (eV)	−7.15	−7.39	−7.19	−7.21	−7.21	−7.19	/	up to −7.20

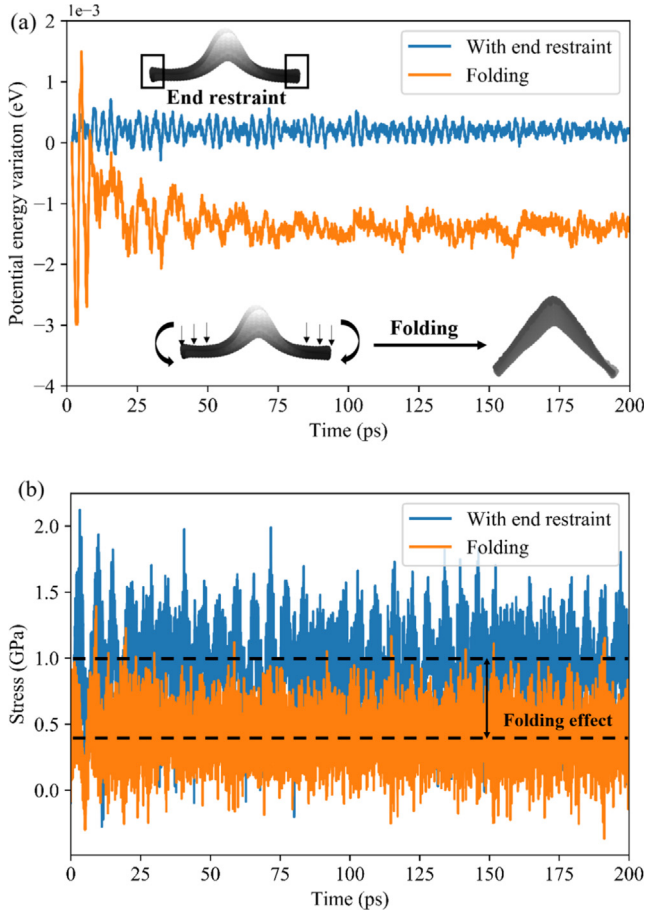

Fig. 8. Direct evidence of high self-assembly capacity regarding folding effect. (a) Potential energy variation as a function of simulation time. In particular, the self-assembly graphene unit cell with end restrained and the spontaneous folding of self-assembly graphene are considered to reflect the folding effect. There is a remarkable gap between their potential curves. (b) Evolution of stress along the direction of Burgers vector for self-assembly graphene unit cell. (A colour version of this figure can be viewed online.)

graphene with topological defects can bring considerable folding effect. Fortunately, we successfully observe the significant effect. The variation in potential energy and stress are clearly plotted in Fig. 8(a) and (b), respectively. It is evident that the self-assembly graphene unit cell exert a "moment" on outside restraints, i.e., this set of simulation experiment exposes the folding effect of self-assembly graphene.

Additionally, according to Statistical mechanical analysis of warped membranes [51], the renormalized elastic constants scale as

$$\frac{Y_R}{Y} \sim \sqrt{\frac{D}{Yh_v^2}} \tag{9}$$

$$\frac{D_R}{D} \sim \sqrt{\frac{Yh_v^2}{D}} \tag{10}$$

where Y_R and Y are the renormalized Young's modulus and Young's modulus, respectively. D_R and D are the renormalized bending rigidity and bending rigidity, respectively. h_v^2 represents the height profile variance of membranes. Due to significantly geometrical distortion of self-assembly graphene unit cell (see the legends in Fig. 8(a)), the larger bending rigidity and smaller modulus can be realized by the larger h_v^2 of self-assembly graphene unit cell as compared to that of pristine graphene. These obtained results show good agreement with the analysis based on our previous works [52,53] regarding Pseudo Crease (PC) model, i.e., "rippling configuration" of graphene resulting from topological defects or functional groups can affect its elastic properties. Also, in current research, the elastic modulus Y^j ($j = I, II$) scales as

$$Y^j \sim \sqrt{(\varepsilon_j \cos\theta_j)^3} \ (j = I, II) \tag{11}$$

where ε_j and θ_j are initial strain and inclined angle of graphene, respectively. The subscripts $j = I$ and $j = II$ represent the corresponding parameters perpendicular to the Burgers vector and parallel to the Burgers vector, respectively. Because of $\varepsilon_I > \varepsilon_{II}$ and $\theta_I < \theta_{II}$ (based on our simulation experiments), it is apparent that the elastic modulus perpendicular to the direction of Burgers vector is larger than the elastic modulus parallel to the direction of Burgers vector, $Y^I > Y^{II}$. This difference is conducive to the mechanical abnormality design and programmable design of graphene with topological defects.

To validate those interesting findings, the related elastic properties of the self-assembly graphene unit cell are compared with the values from the open literatures in Table 2. The larger bending rigidity (almost one order larger than that of pristine graphene) and smaller modulus of self-assembly graphene can be achieved. The results from the calculations and experiments are agreement with our theoretical analysis, proving that our prediction is correct and can provide insights into the rational design and practice of self-assembly graphene with surface topological defects.

4.3. Self-assembly graphene container as a potential drug delivery device

Before concluding, we outline the potential application of drug delivery device towards the self-assembly graphene. It is well known that non-covalently linked core-shell systems, such as the drug delivery systems, are being overwhelmingly canonized as such systems allow hydrophobic therapeutic drug to be encapsulated inside the core and the graphene shell separates it from the external hydrophilic environment [57]. Therefore, we refine the approach by surface design of topological defects and develop the self-assembly mode based on geometry effects (as well as topological effects) of topological defects. On the basis of self-assembly phase diagrams in Fig. 4(b) and self-assembly capacity from the building block, here we demonstrate the highly parallel self-assembly process in relation to formation of nanocontainers and encapsulation of therapeutic drugs. It is noteworthy that although self-assembly graphene is dominant to encapsulate the therapeutic drug, there is, in fact, much evidence to indicate that achieving high drug encapsulation capacity requires the synergy of three

Table 2
Comparison of elastic properties for self-assembly graphene unit cell and pristine graphene. The calculation and simulation details are provided in S10.

Elastic modulus (TPa)	Bending rigidity (eV)	Poison's ratio	Reference	Remarks
0.69^I	13.67^I	0.11^I	This study	Self-assembly graphene (theory and atomistic simulation, direction *I*)
0.32^{II}	6.65^{II}	0.09^{II}	This study	Self-assembly graphene (theory and atomistic simulation, direction *II*)
0.96^a, 0.88^z	1.14	0.16^a, 0.14^z	This study	Graphene (theory and atomistic simulation, armchair and zigzag)
1.03	/	/	[2]	Graphene (experiment)
1.01	1.49	0.15	[54]	Graphene (DFT calculation)
1	1.1	0.16	[55]	Graphene (atomistic simulation)
1.05	1.2	0.19	[56]	Graphene (experiment, DFT calculation)

interaction effects: one involving the self-assembly graphene, one involving the vdW interaction between self-assembly graphene and therapeutic drugs, and one regarding the offset π-π stacking interaction between theirs [13]. Traditionally, the vdW interaction is the fundamental driving force for self-assembly based on surface tension mechanism. However, high specific π-π stacking can be exploited to achieve high drug loading of poorly soluble particles without compromising potency or efficiency. Combining these interaction effects, the mechanism of self-assembly significantly expands the ability of existing self-assembly drug delivery devices and opens an avenue for the design of next generation of drug delivery systems. Based on thermodynamics principle and systematic simulation experiments, we investigate the feasibility of graphene with surface topological defects for drug delivery device. The binding energy between self-assembly graphene and therapeutic drugs (i.e., non-covalently linked core–shell systems) can be expressed as $E_{Binding} = -\sigma_{Binding} A_{Binding} < 0$ where $\sigma_{Binding}$ is the density of binding energy, $A_{Binding}$ is the binding area. The deformation energy of self-assembly graphene can be given by $E_{Deformation} = -\sigma_{Deformation} A_{Deformation} < 0$ where $\sigma_{Deformation}$ represents the density of strain energy, $A_{Deformation}$ represents equivalent area of self-assembly graphene. A very simple but profound result in relation to energy condition can be further determined, as follows

$$E_{Binding} + E_{Deformation} < 0 \tag{12}$$

where the negativity of Eq. (12) is always satisfied during the self-assembly process for drug delivery. This indicates that as soon as simulation experiment starts, the self-assembly graphene/drug system will tend to become more stable. However, compared to those comparable results, especially with respect to self-assembly drug delivery system based on surface tension mechanism, Eq. (12) is not always satisfied during the self-assembly process due to the positive deformation energy of graphene $E_{Deformation} > 0$ [18,46,58]. Therefore, our design of self-assembly graphene container for drug delivery is more effective, which the results from theoretical analysis (see Eq. (12)) and simulation experiment (see Fig. 2(f) and Fig. 3(g)) make it clear that the potential drug encapsulation in our research is very promising. The simulation results of highly parallel self-assembly process in relation to formation of nanocontainers and encapsulation of particle are also provided, as we can see from Fig. S11. Additionally, the folding effect from geometry and topology effect of topological defects (see Figs. S6 and S7) can be used for explicating configuration shift phenomenon in Ref. [22], as we provided in S12.

5. Conclusions

In summary, we introduced an effective design strategy motivated by experiments for the self-assembly graphene with surface topological defects, and explored the self-assembly behaviors by considering 54 morphologies with various design variables based on the extensive atomistic simulations. We construct the self-assembly phase diagrams with some counterintuitive expectations to guide the rational selection of design variables to design the novel nanostructures through high parallel self-assembly process. Some remarkable conclusions are as follows:

1. The knowledge of the design principles and self-assembly phase diagrams for their morphology thresholds $N_{Threshold\text{-}1}$, $N_{Threshold\text{-}2}$ and $N_{Threshold\text{-}3}$ can serve as an important theory in speed-up of searching the novel nanostructures and allotropes;
2. The self-assembly phase diagrams are found to break the governing mechanism for geometry-controlled configuration of graphene. Correspondingly, four modes involving polygon nanoscroll ($N > N_{Threshold\text{-}3}$), polygon nanotube ($N_{Threshold\text{-}2} > N > N_{Threshold\text{-}3}$), breathing oscillation ($N_{Threshold\text{-}2} > N > N_{Threshold\text{-}1}$) and damping vibration ($N < N_{Threshold\text{-}1}$) can be identified;
3. It can be straightforward to reverse engineer a graphene surface with surface topological defects to approximate a target geometry such as polygon nanoscroll and polygon nanotube. In particular, the triangle, square, pentagon and hexagon (i.e. N gon) nanotubes can be formed based on the self-assembly construction, indicating that graphene origami can be realized;
4. The influence of energy conversion and energy dissipation is found to be more dominant resulting in breathing oscillation and damping vibration;
5. Insights from the fundamental building block of self-assembly graphene suggest that larger deformation energy, larger bending rigidity and smaller modulus can be realized. The folding effect, as the direct evidence of self-assembly capacity, can exert a “moment” on outside restraints. Based on these findings, feasibility of drug delivery device can be demonstrated theoretically.

Declaration of Competing Interest

The authors declared that there is no conflict of interest.

Acknowledgements

The authors gratefully acknowledge financial supports from National Natural Science Foundation of China, 11872160 and 11572099.

The author wishes to thank Mrs. Zaiying Zhang and Mr. Gongran Wang for their thoughtful kindness.

Appendix A. Supplementary material

Supplementary data to this article can be found online at https://doi.org/10.1016/j.apsusc.2019.144008.

References

[1] H.I. Rasool, C. Ophus, W.S. Klug, A. Zettl, J.K. Gimzewski, Measurement of the intrinsic strength of crystalline and polycrystalline graphene, Nat. Commun. 4 (2013).
[2] C. Lee, X. Wei, J.W. Kysar, J. Hone, Measurement of the elastic properties and intrinsic strength of monolayer graphene, Science 321 (2008) 385–388.
[3] J.S. Bunch, A.M. van der Zande, S.S. Verbridge, I.W. Frank, D.M. Tanenbaum, J.M. Parpia, H.G. Craighead, P.L. McEuen, Electromechanical resonators from graphene sheets, Science 315 (2007) 490–493.
[4] A.A. Balandin, S. Ghosh, W. Bao, I. Calizo, D. Teweldebrhan, F. Miao, C.N. Lau, Superior thermal conductivity of single-layer graphene, Nano Lett. 8 (2008) 902–907.
[5] M.Z. Miskin, K.J. Dorsey, B. Bircan, Y. Han, D.A. Muller, P.L. McEuen, I. Cohen, Graphene-based bimorphs for micron-sized, autonomous origami machines, PNAS 115 (2018) 466–470.
[6] O.K. Park, C.S. Tiwary, Y. Yang, S. Bhowmick, S. Vinod, Q. Zhang, V.L. Colvin, S.A.S. Asif, R. Vajtai, E.S. Penev, B.I. Yakobson, P.M. Ajayan, Magnetic field controlled graphene oxide-based origami with enhanced surface area and mechanical properties, Nanoscale 9 (2017) 6991–6997.
[7] S. Koch, D. Stradi, E. Gnecco, S. Barja, S. Kawai, C. Diaz, M. Alcami, F. Martin, A.L. Vazquez de Parga, R. Miranda, T. Glatzel, E. Meyer, Elastic response of graphene nanodomes, ACS Nano 7 (2013) 2927–2934.
[8] D. Lahiri, S. Das, W. Choi, A. Agarwal, Unfolding the damping behavior of multilayer graphene membrane in the low-frequency regime, ACS Nano 6 (2012) 3992–4000.
[9] W. Chen, P. Xiao, H. Chen, H. Zhang, Q. Zhang, Y. Chen, Polymeric graphene bulk materials with a 3D cross-linked monolithic graphene network, Adv. Mater. (2018) e1802403.
[10] S. Zhu, T. Li, Hydrogenation-assisted graphene origami and its application in programmable molecular mass uptake, storage, and release, ACS Nano 8 (2014) 2864–2872.
[11] S. Boothroyd, J. Anwar, Conceptual, self-assembling graphene nanocontainers, Nanoscale 7 (2015) 12104–12108.
[12] L. Zhang, X. Zeng, X. Wang, Programmable hydrogenation of graphene for novel nanocages, Sci. Rep. 3 (2013) 3162.
[13] S. Goenka, V. Sant, S. Sant, Graphene-based nanomaterials for drug delivery and tissue engineering, J. Control. Release 173 (2014) 75–88.
[14] N. Patra, B. Wang, P. Kral, Nanodroplet activated and guided folding of graphene nanostructures, Nano Lett. 9 (2009) 3766–3771.
[15] R. Tkacz, R. Oldenbourg, A. Fulcher, M. Miansari, M. Majumder, Capillary-Force-Assisted Self-Assembly (CAS) of highly ordered and anisotropic graphene-based thin films, J. Phys. Chem. C 118 (2013) 259–267.

[16] H.T. Kieu, B. Liu, H. Zhang, K. Zhou, A.W.-K. Law, Molecular dynamics study of water evaporation enhancement through a capillary graphene bilayer with tunable hydrophilicity, Appl. Surf. Sci. 452 (2018) 372–380.
[17] K. Cai, J. Wan, J. Yu, H. Cai, Q. Qin, Molecular dynamics study on welding a defected graphene by a moving fullerene, Appl. Surf. Sci. 377 (2016) 213–220.
[18] S. Huang, M. Feng, B. Wang, X. Xu, X. Cao, Y. Wang, Molecular dynamics simulation on the fabrication of graphene nanoscrolls with ferromagnetic nanowire templates, Appl. Surf. Sci. 347 (2015) 162–168.
[19] S. Zhu, T. Li, Hydrogenation enabled scrolling of graphene, J. Phys. D 46 (2013) 075301.
[20] Z. Hasanzade, H. Raissi, Solvent/co-solvent effects on the electronic properties and adsorption mechanism of anticancer drug Thioguanine on Graphene oxide surface as a nanocarrier: density functional theory investigation and a molecular dynamics, Appl. Surf. Sci. 422 (2017) 1030–1041.
[21] D.C. Elias, R.R. Nair, T.M. Mohiuddin, S.V. Morozov, P. Blake, M.P. Halsall, A.C. Ferrari, D.W. Boukhvalov, M.I. Katsnelson, A.K. Geim, K.S. Novoselov, Control of graphene's properties by reversible hydrogenation: evidence for graphene, Science 323 (2009) 610–613.
[22] J.H. Warner, Y. Fan, A.W. Robertson, K. He, E. Yoon, G.D. Lee, Rippling graphene at the nanoscale through dislocation addition, Nano Lett. 13 (2013) 4937–4944.
[23] T. Zhang, X. Li, H. Gao, Defects controlled wrinkling and topological design in graphene, J. Mech. Phys. Solid 67 (2014) 2–13.
[24] M. Becton, X. Wang, Tailoring patterns of graphene wrinkles by circular torsion, Appl. Surf. Sci. 363 (2016) 13–20.
[25] Y. Wang, Z. Liu, Spontaneous rolling-up and assembly of graphene designed by using defects, Nanoscale (2018).
[26] A. Sgouros, M.M. Sigalas, K. Papagelis, G. Kalosakas, Transforming graphene nanoribbons into nanotubes by use of point defects, J. Phys. Condens. Mater. 26 (2014) 125301.
[27] O.V. Yazyev, S.G. Louie, Topological defects in graphene: Dislocations and grain boundaries, Phys. Rev. B 81 (2010).
[28] Z. Song, Z. Xu, Topological defects in two-dimensional crystals: the stress buildup and accumulation, J. Appl. Mech. 81 (2014) 091004.
[29] Z. Zhang, A. Kutana, A. Roy, B.I. Yakobson, Nanochimneys: topology and thermal conductance of 3D nanotube-graphene cone junctions, J. Phys. Chem. C 121 (2017) 1257–1262.
[30] S. Plimpton, Fast parallel algorithms for short-range molecular-dynamics, J. Comput. Phys. 117 (1995) 1–19.
[31] S.J. Stuart, A.B. Tutein, J.A. Harrison, A reactive potential for hydrocarbons with intermolecular interactions, J. Chem. Phys. 112 (2000) 6472–6486.
[32] Z.G. Song, V.I. Artyukhov, J. Wu, B.I. Yakobson, Z.P. Xu, Defect-detriment to graphene strength is concealed by local probe: the topological and geometrical effects, ACS Nano 9 (2015) 401–408.
[33] C. Wang, Y. Liu, L. Lan, H. Tan, Graphene wrinkling: formation, evolution and collapse, Nanoscale 5 (2013) 4454–4461.
[34] Y.F. Wang, C.G. Wang, Y.C. Zhang, J.M. Guo, H.F. Tan, Dimensional variation of reconfigurable serpentine graphene nanoribbon under tension, J. Appl. Phys. 125 (2019).
[35] Y. Liu, B.I. Yakobson, Cones, pringles, and grain boundary landscapes in graphene topology, Nano Lett. 10 (2010) 2178–2183.
[36] H. Qin, Y. Sun, J.Z. Liu, Y. Liu, Mechanical properties of wrinkled graphene generated by topological defects, Carbon 108 (2016) 204–214.
[37] Y. Wang, C. Wang, Y. Zhang, H. Tan, Graphene kirigami as reinforcement and interfacial bonding effect for toughness and strength of silicon-based nanocomposites, Comput. Mater. Sci. 159 (2019) 306–315.
[38] Y. Wang, C. Wang, H. Tan, Intrinsic edge warping of graphene nanoribbon boost molecular directional motion: toward the novel nanodevices, Phys. Lett. A 383 (2019) 1473–1477.
[39] J. Wu, H. Zhao, J. Liu, Z. Zhang, F. Ning, Y. Liu, Nanotube-chirality-controlled tensile characteristics in coiled carbon metastructures, Carbon 133 (2018) 335–349.
[40] O.A. Shenderova, D.W. Brenner, A. Omeltchenko, X. Su, L.H. Yang, Atomistic modeling of the fracture of polycrystalline diamond, Phys. Rev. B 61 (2000) 3877–3888.
[41] C.W. Pao, T.H. Liu, C.C. Chang, D.J. Srolovitz, Graphene defect polarity dynamics, Carbon 50 (2012) 2870–2876.
[42] Z. Xu, M.J. Buehler, Geometry controls conformation of graphene sheets: membranes, ribbons, and scrolls, ACS Nano 4 (2010) 3869–3876.
[43] J.C. Meyer, A.K. Geim, M.I. Katsnelson, K.S. Novoselov, T.J. Booth, S. Roth, The structure of suspended graphene sheets, Nature 446 (2007) 60–63.
[44] H.E. Lim, Y. Miyata, R. Kitaura, Y. Nishimura, Y. Nishimoto, S. Irle, J.H. Warner, H. Kataura, H. Shinohara, Growth of carbon nanotubes via twisted graphene nanoribbons, Nat. Commun. 4 (2013) 2548.
[45] A. Chuvilin, E. Bichoutskaia, M.C. Gimenez-Lopez, T.W. Chamberlain, G.A. Rance, N. Kuganathan, J. Biskupek, U. Kaiser, A.N. Khlobystov, Self-assembly of a sulphur-terminated graphene nanoribbon within a single-walled carbon nanotube, Nat. Mater. 10 (2011) 687–692.
[46] J.W. Feng, H.M. Ding, Y.Q. Ma, Self-assembly of fullerenes and graphene flake: A molecular dynamics study, Carbon 90 (2015) 34–43.
[47] C. Wang, Y. Liu, L. Li, H. Tan, Anisotropic thermal conductivity of graphene wrinkles, Nanoscale 6 (2014) 5703–5707.
[48] A. Fasolino, J.H. Los, M.I. Katsnelson, Intrinsic ripples in graphene, Nat. Mater. 6 (2007) 858–861.
[49] X.H. Shi, N.M. Pugno, Y. Cheng, H.J. Gao, Gigahertz breathing oscillators based on carbon nanoscrolls, Appl. Phys. Lett. 95 (2009).
[50] C.G. Wang, L. Lan, Y.P. Liu, H.F. Tan, X.D. He, Vibration characteristics of wrinkled single-layered graphene sheets, Inter. J. Solid Struct. 50 (2013) 1812–1823.
[51] A. Kosmrlj, D.R. Nelson, Mechanical properties of warped membranes, Phys. Rev. E 88 (2013) 012136.
[52] Z.M. Xia, C.G. Wang, H.F. Tan, Strain-dependent elastic properties of graphene oxide and its composite, Comp. Mater. Sci. 150 (2018) 252–258.
[53] Z.M. Xia, C.G. Wang, H.F. Tan, Elastoplastic folding behavior of membrane ribbon based on plane strain beam theory, Inter. J. Solid. Struct. 143 (2018) 167–174.
[54] K.N. Kudin, G.E. Scuseria, B.I. Yakobson, C2F, BN, and C nanoshell elasticity from abinitio computations, Phys. Rev. B 64 (2001).
[55] J.H. Los, L.M. Ghiringhelli, E.J. Meijer, A. Fasolino, Improved long-range reactive bond-order potential for carbon. I. Construction, Phys. Rev. B 72 (2005).
[56] Y. Wei, B. Wang, J. Wu, R. Yang, M.L. Dunn, Bending rigidity and Gaussian bending stiffness of single-layered graphene, Nano Lett. 13 (2013) 26–30.
[57] J. Li, D.J. Mooney, Designing hydrogels for controlled drug delivery, Nat. Rev. Mater. 1 (2016).
[58] Y. Li, H. Li, K. Zhang, K.M. Liew, The theoretical possibility of a graphene sheet spontaneously scrolling round an iron nanowire, Carbon 50 (2012) 566–576.